

See discussions, stats, and author profiles for this publication at: <https://www.researchgate.net/publication/254263478>

# Non-Antireflective Scheme for Efficiency Enhancement of Cu(In,Ga)Se<sub>2</sub> Nanotip Arrays Solar Cells.

ARTICLE in ACS NANO · AUGUST 2013

Impact Factor: 12.88 · DOI: 10.1021/nn402976b · Source: PubMed

CITATIONS

8

READS

26

16 AUTHORS, INCLUDING:



Jenh-Yih Juang

National Chiao Tung University

261 PUBLICATIONS 1,535 CITATIONS

SEE PROFILE



Kh Wu

National Chiao Tung University

172 PUBLICATIONS 839 CITATIONS

SEE PROFILE



Shun-Jen Cheng

National Chiao Tung University

72 PUBLICATIONS 740 CITATIONS

SEE PROFILE



Hao-Chung Kuo

National Chiao Tung University

771 PUBLICATIONS 6,428 CITATIONS

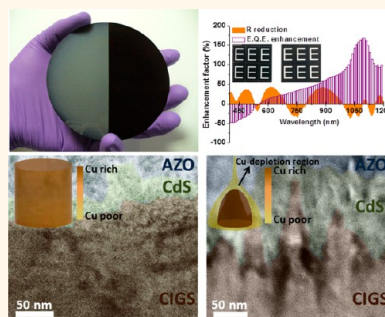
SEE PROFILE

# Non-antireflective Scheme for Efficiency Enhancement of Cu(In,Ga)Se<sub>2</sub> Nanotip Array Solar Cells

Yu-Kuang Liao,<sup>‡</sup> Yi-Chung Wang,<sup>§</sup> Yu-Ting Yen,<sup>§</sup> Chia-Hsiang Chen,<sup>§</sup> Dan-Hua Hsieh,<sup>†</sup> Shih-Chen Chen,<sup>‡</sup> Chia-Yu Lee,<sup>‡</sup> Chih-Chung Lai,<sup>§</sup> Wei-Chen Kuo,<sup>‡</sup> Jenh-Yi Juang,<sup>‡</sup> Kaung-Hsiung Wu,<sup>‡</sup> Shun-Jen Cheng,<sup>‡</sup> Chih-Huang Lai,<sup>§</sup> Fang-I Lai,<sup>⊥</sup> Shou-Yi Kuo,<sup>||</sup> Hao-Chung Kuo,<sup>†,\*</sup> and Yu-Lun Chueh<sup>§,\*</sup>

<sup>†</sup>Department of Photonics and Institute of Electro-optical Engineering and <sup>‡</sup>Department of Electro-physics, National Chiao-Tung University, Hsinchu, 30010, Taiwan, Republic of China, <sup>§</sup>Department of Materials Science and Engineering, National Tsing-Hua University, Hsinchu 30013, Taiwan, Republic of China, <sup>⊥</sup>Department of Photonic Engineering, Yuan-Ze University, Taoyuan 32003, Taiwan, Republic of China, and <sup>||</sup>Department of Electronic Engineering, Chang-Gung University, Taoyuang 33302, Taiwan, Republic of China

**ABSTRACT** We present systematic works in characterization of CIGS nanotip arrays (CIGS NTRs). CIGS NTRs are obtained by a one-step ion-milling process by a direct-sputtering process of CIGS thin films (CIGS TF) without a postselenization process. At the surface of CIGS NTRs, a region extending to 100 nm in depth with a lower copper concentration compared to that of CIGS TF has been discovered. After KCN washing, removal of secondary phases can be achieved and a layer with abundant copper vacancy ( $V_{Cu}$ ) was left. Such compositional changes can be a benefit for a CIGS solar cell by promoting formation of Cd-occupied Cu sites ( $Cd_{Cu}$ ) at the CdS/CIGS interface and creates a type-inversion layer to enhance interface passivation and carrier extraction. The raised  $V_{Cu}$  concentration and enhanced Cd diffusion in CIGS NTRs have been verified by energy dispersive spectrometry. Strengthened adhesion of Al:ZnO (AZO) thin film on CIGS NTRs capped with CdS has also been observed in SEM images and can explain the suppressed series resistance of the device with CIGS NTRs. Those improvements in electrical characteristics are the main factors for efficiency enhancement rather than antireflection.



**KEYWORDS:** CIGS solar cell · direct sputtering · nanotip arrays · copper vacancy · Cd diffusion

Combustible fuel is an energy source that has always been heavily relied on to power the world. Yet, a side product, greenhouse gas, has been produced at the same time and now results in hazardous climate change. Impacts of more severe weather crises are possible if alternative replacements of clean, environment-friendly, and sustainable energy sources are not generalized. Renewable energy has continually been dramatically expanded in the past decade and is expected to grow even faster in the future. Photovoltaics (PV), namely, solar cells, is one of the primary sources of renewable energy due to its adaptability to different locations, which therefore allows versatile uses. Compared to wafer-based silicon solar cells, thin film solar cells possess the advantage of low cost in raw material, which gives them a prospective cost-down scenario by manufacturing development, which is very advantageous for industry. Among all solar cells, chalcopyrite

Cu(In,Ga)Se<sub>2</sub> (CIGS) thin film solar cell have been regarded as one of the most promising thin film solar cells due to their high efficiency, low cost, and easy integration with current Si-based processes.<sup>1</sup>

A recorded efficiency of CIGS solar cells of up to 20.4% has been achieved by EMPA, which gives CIGS solar cells a reputation as a high potential candidate among energy alternatives.<sup>2</sup> Much effort has been devoted to develop various deposition methods for the absorber layer in past decades, including conventional co-evaporation,<sup>3</sup> sputtering with postselenization processes,<sup>4</sup> ink-printing,<sup>5</sup> and electrochemical deposition.<sup>6</sup> Except for co-evaporation, almost all deposition methods need the postselenization process, which is a critical barrier for high throughput. A method of direct sputtering from a quaternary CIGS target without postselenization has been demonstrated to address the tedious obstructions of selenization and meet the demands of large throughput and scale-up.<sup>7</sup>

\* Address correspondence to ylchueh@mx.nthu.edu.tw (Y.-L. Chueh), hckuo@faculty.nctu.edu.tw (H.-C. Kuo).

Received for review June 12, 2013 and accepted August 1, 2013.

Published online August 01, 2013  
10.1021/nn402976b

© 2013 American Chemical Society

Until a solar cell that accesses the theoretical efficiency limit can be fabricated, reduction in Fresnel reflection at the interface between air and the device is always an essential approach to boost the efficiency. In order to reduce reflection, a conventional way of depositing a thin film onto solar cells to suppress reflectance, namely, an antireflection coating (ARC) technique, has been widely utilized. It yet has also resulted in trade-offs, such as reliability degradation due to thermal mismatch between the ARC layer and the device, as well as significantly raising the cost due to the vacuum fabrication process.<sup>8,9</sup>

Astonishing nanoscale architectures that have a perfect antireflection effect have been discovered.<sup>10</sup> Conical arrays are well known as the best morphology to completely suppress Fresnel reflection at the surface due to the concept of gradual refractive index, which has been theoretically and experimentally demonstrated by several research groups with tapered or vertically conical-shaped structures.<sup>11</sup> To date, a great variety of fabrication methods for different antireflectance nanostructures have been well established.<sup>12–17</sup> However, most of them need multiple processes, which lower the throughput and yield, thereby raising the cost. As a solution to this issue, a low-cost, template-free, nontoxic, large-area, rapid-throughput, and uniform CIGS nanotip array (CIGS NTR) generated through a direct and one-step ion-milling process on CIGS thin films (CIGS TF) has been demonstrated.<sup>18</sup> The particular technique not only brings remarkable efficiency enhancement but also combines both high-yield and low-cost benefits, which demonstrates a low-cost nanostructure technology.<sup>18</sup> CIGS NTR solar cells have shown a magnificent efficiency enhancement that is way beyond what most nanostructured CIGS solar cells have achieved.<sup>19</sup> Yet, since the scheme of CIGS NTRs is to embed a CIGS nanostructure inside the device, by which a CdS buffer layer and transparent conductive oxide (TCO) layer capping the top can provide ARCs with step-decreased refraction indices, the antireflection property of CIGS NTRs should be quenched by ARCs as well as the high absorption at the CIGS absorber layer and results in less enhancement of efficiency by antireflection. What is more, by taking CIGS solar cells without CIGS NTRs as a reference, CIGS solar cells with CIGS NTRs exhibit enhanced open circuit voltage ( $V_{OC}$ ) and fill factor (FF), which is what antireflection alone has not been able to achieve.<sup>12–17</sup> As a result, the actual mechanism of the great efficiency enhancement by CIGS NTRs is still ambiguous and has not yet been investigated. In this regard, the enhanced efficiency mechanism of this new CIGS NTR was systematically investigated by photoluminescence (PL), time-resolved photoluminescence (TRPL), and energy dispersion spectrometry (EDS). Interestingly, the results have exhibited that the efficiency enhancement achieved by CIGS NTRs is NOT the main attribution to

antireflection as the conventional scheme of the nanostructure. It has ultimately been discovered that an elemental concentration change at the surface of CIGS NTRs caused by ion-milling is what has boosted the efficiency, by which a decreased shunt leakage of the device can be achieved. In addition, a better adhesion of an Al:ZnO (AZO) thin film to CIGS NTRs capped with CdS has also been observed. Suppression in series resistance of the device with CIGS NTRs, hence enhancement in device efficiency, has also been observed and discussed in -depth.

## RESULTS AND DISCUSSION

Figure 1(a)–(d) show SEM images of CIGS TF and CIGS NTRs before and after KCN solution treatment. When a direct-sputtered CIGS TF was initially prepared, secondary phases and copper-rich CIGS were formed simultaneously due to copper segregation, which could cause shunt leakage as illustrated in Figure 1(a); therefore the conventional removal method of a secondary phase by immersing the CIGS in KCN solution is an imperative step for a high-efficiency CIGS solar cell. The KCN-solution-treated CIGS TF is shown in Figure 1(b), in which no significant morphology change was observed.

Figure 1(c) shows CIGS NTRs with a height around 200 nm after the one-step ion-milling process, by which the Cu segregation and Cu-rich CIGS phases were severely deformed; therefore coalescence between tips can be seen. After KCN treatment, sharp CIGS NTRs can be formed due to removal of extra secondary phases, as shown in Figure 1(d). The corresponding TEM images of the CIGS TF and the CIGS NTRs after KCN treatment are shown in Figure 1(e) and (f). The inset in Figure 1(e) taken from a rectangular area in Figure 1(e) shows a high-resolution TEM image, with which an internal spacing of 0.3 nm corresponding to a (112) plane and selective diffraction pattern [201] zone axis can be indexed. On the other hand, CIGS NTRs also exhibit a single-crystal feature with the same lattice plane and selected diffraction pattern, confirmed by the high-resolution TEM image shown in Figure 1(f).

The CIGS NTR formation *via* the ion-milling process can be understood through the theoretical interpretation of ion bombardment, indicating a surface atomic diffusion taking place *via* a collision cascade, a process of sequential collisions of atoms, ignited by external ion bombardment while ion-milling.<sup>20–22</sup> Patterns with high aspect ratio were initially regarded to be hardly formed by ion bombardment due to the fact that erosion at the surface should be suppressed by surface diffusion and the surface morphology remains at an equilibrium status. The following research has shown that the self-assembled sacrificial mask formed by phase segregation allows patterns of high aspect ratio, resulting in formation of CIGS NTRs.<sup>18</sup> Based on the theory of spinodal decomposition in an alloy, there

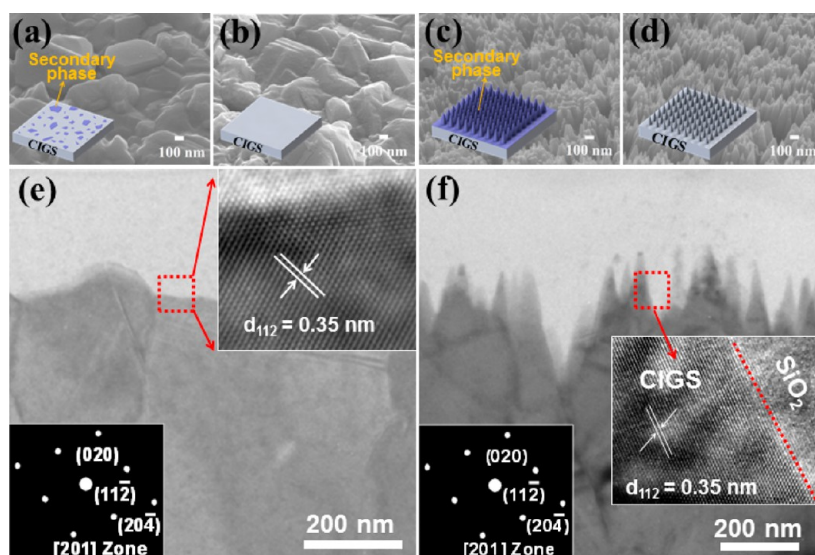


Figure 1. SEM images of (a) CIGS TF before KCN washing, (b) CIGS TF after KCN washing, (c) CIGS NTRs before KCN washing, (d) CIGS NTRs after KCN washing. Insets in (a) to (d) show the corresponding schematic illustrations of the samples. (e) TEM image of CIGS TF after KCN washing. (f) High-resolution TEM image of CIGS NTRs after KCN washing. Insets in (e) and (f) show the corresponding high-resolution TEM images and selective diffraction patterns.

has developed an adaptable explanation of phase separation induced by ion bombardment in a multiple atomic composition system.<sup>23–25</sup> The theory shows that a collision cascade has extended atomic diffusion into the CIGS bulk by surface energy and brings phase re-formation throughout the extended region. In a Cu–In–Se system, a Cu-rich secondary phase has a lower formation energy than that of the desired chalcopyrite phase for solar cells so that a secondary phase can stably exist under a rather lower growth temperature within a certain range of given Cu concentration. Therefore a Cu-rich secondary phase is more likely to be re-formed in the atomic diffusion region. This explains the abundant Cu-rich phases at the surface of CIGS NTRs. By taking phase re-formation at the CIGS surface into account, considerable composition evolution is possible during ion-milling.

A demonstration of larger scale CIGS NTRs and resultant devices are shown in Figure 2. Figure 2(a) shows a photograph of a 4-in. direct-sputtered CIGS wafer, in which CIGS NTRs were fabricated on the right half of the wafer. An obvious antireflection effect can be seen from the significant color contrast between the two halves. Yet, the resultant CIGS solar cells show otherwise. Figure 2(b) shows two direct-sputtering CIGS solar cells, with the right one embedded with CIGS NTRs. An antireflection effect can still be observed, but is ambiguous. Reflectance of the CIGS absorber layer and CIGS solar cells with and without CIGS NTRs has been measured for clarification. Figure 2(c) shows the reflectance spectra of CIGS TF and the CIGS NTR absorber layer. As expected, CIGS NTRs exhibit a significantly low reflectance spectrum, compared to that of CIGS TF. However, such reflectance contrast was diminished after CIGS TF and CIGS NTRs were fabricated

into devices, as shown in Figure 2(d), in which the reflectance spectra of the devices with and without CIGS NTRs are similar.

Figure 3(a) and (b) show the  $J$ – $V$  curves and external quantum efficiency (EQE) spectra of CIGS TF and CIGS NTR devices. An improved performance of the CIGS NTR device has been verified by comparison to that of the CIGS TF device. CIGS NTRs have achieved an efficiency enhancement of 56.25% (from 2.88% to 4.50%) with enhanced  $V_{OC}$ , FF, and  $J_{SC}$ , which are boosted from 0.36 to 0.40 V in  $V_{OC}$ , from 49% to 57% in FF, and from 6.55 to 7.90 mA/cm<sup>2</sup> in  $J_{SC}$ , respectively. Not only  $J_{SC}$ , but both  $V_{OC}$  and FF are enhanced, inferring a non-antireflection improvement mechanism. To clarify the doubt, quantitative EQE enhancement and reflection reduction of the devices are compared to each other, in which the EQE enhancement was calculated by  $[(EQE_{NTRs} - EQE_{TF})/EQE_{TF}] \times 100\%$ , and reflectance reduction is calculated by  $[(R_{TF} - R_{NTRs})/R_{TF}] \times 100\%$ . Interestingly, for the device with CIGS NTRs, reflectance reduction is obviously much greater than the enhancement in EQE, as shown in Figure 3(c). Note that the EQE of the CIGS NTR device at wavelengths < 550 nm is lower than that of the CIGS TF device. This is attributed to the 100 nm thick CdS layer used in the CIGS NTRs device, which is thicker than that used in the CIGS TF (usually 50 nm thick CdS layer) device due to efficiency optimization. It is now clear that the remarkable efficiency boost is NOT mainly due to antireflection. To shed light on the mechanism of efficiency boost, energy dispersion spectrometry and photoluminescence of CIGS TF and CIGS NTRs are conducted.

Depth-resolved quantitative compositional distributions of CIGS TF and NTRs samples were performed by EDS. The resultant elemental distributions of Cu, In, Ga,

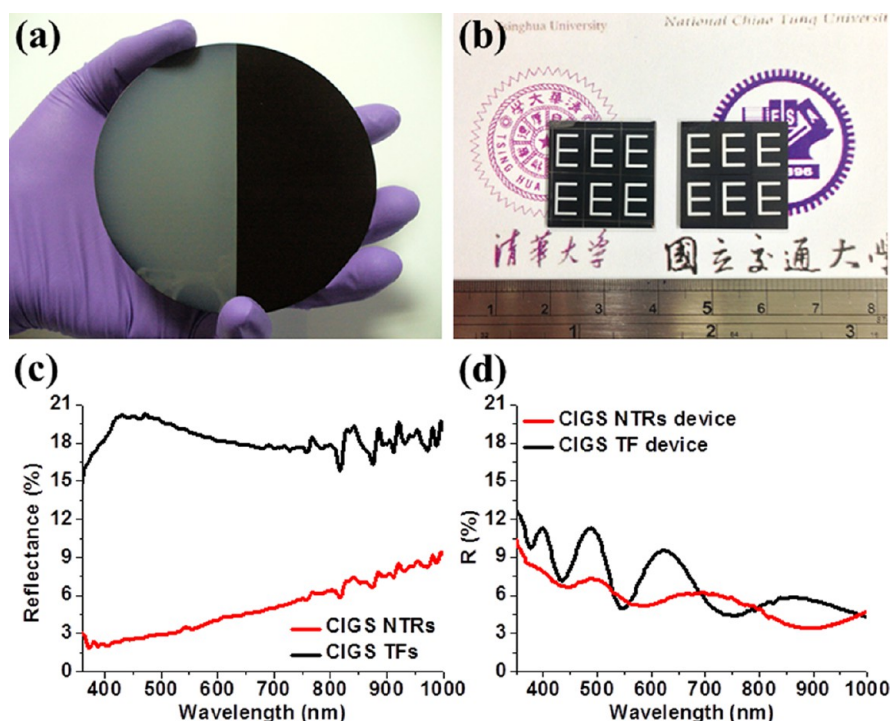


Figure 2. (a) Four-inch CIGS wafer with CIGS NTRs on its right half. (b) Direct-sputtering CIGS solar cells with (right) and without (left) CIGS NTRs. (c) Reflectance spectra of CIGS absorber layer with and without CIGS NTRs. (e) Reflectance spectrum of CIGS solar cells with and without CIGS NTRs.

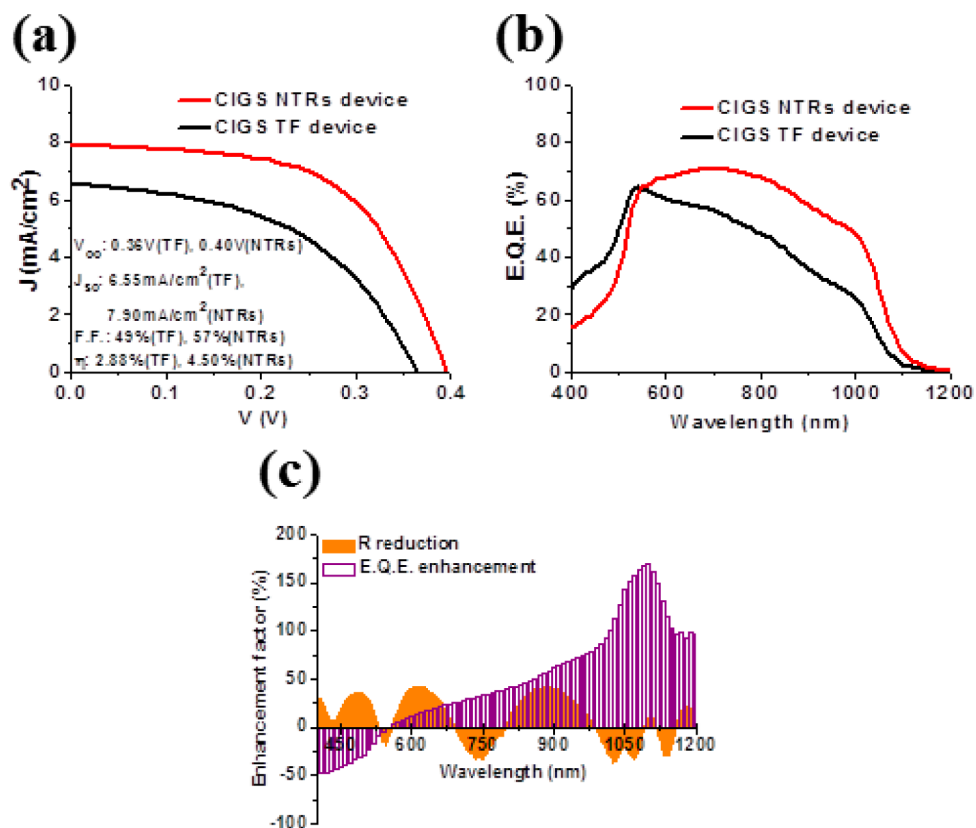


Figure 3. (a)  $J$ - $V$  curve of CIGS solar cells without CIGS NTRs, which is presented as a black line and that with CIGS NTRs, which is presented as a red line. Values of  $V_{oc}$ ,  $J_{sc}$ , FF, and  $\eta$  before and after enhancement are also shown. (b) EQE spectra of a CIGS TF solar cell and a CIGS NTRs solar cell. (c) EQE enhancement and reflectance reduction achieved by CIGS NTRs, in which EQE enhancement is calculated by  $[(EQE_{NTRs} - EQE_{TF})/EQE_{TF}] \times 100\%$  and reflectance reduction is calculated by  $[(R_{TF} - R_{NTRs})/R_{TF}] \times 100\%$ .



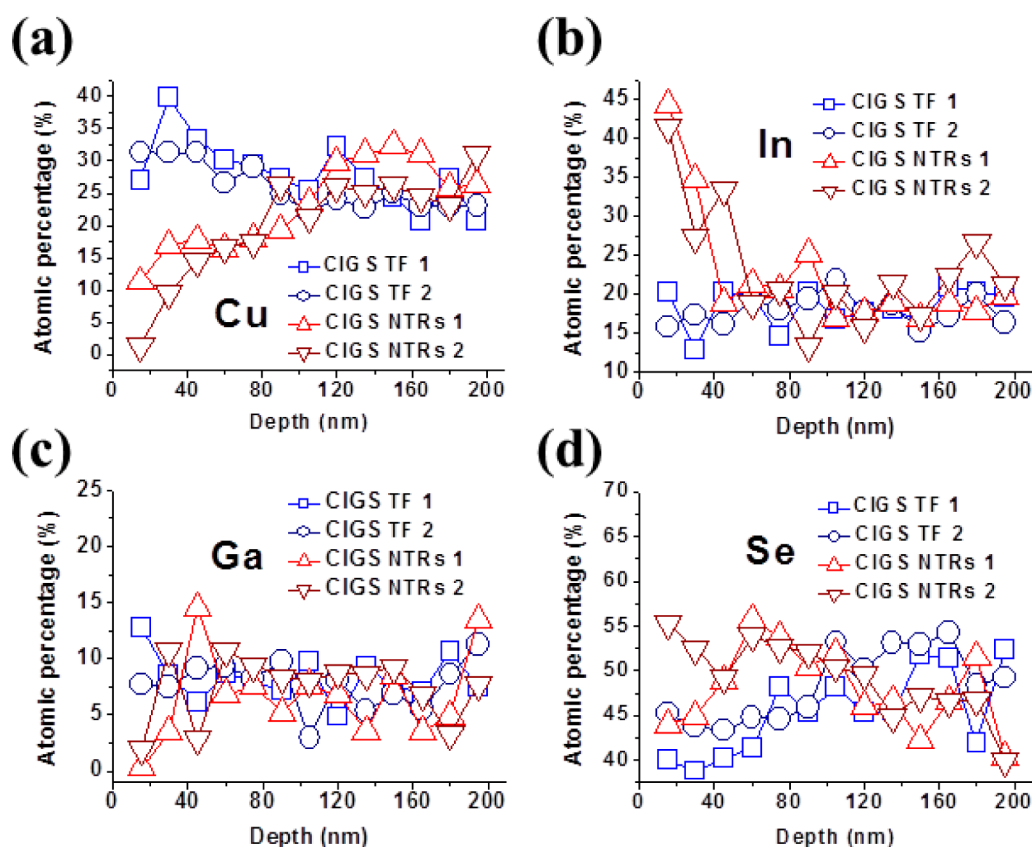


Figure 4. Quantitative analysis obtained by EDS for (a) Cu, (b) In, (c) Ga, and (d) Se in CIGS TF and NTR samples. Two different positions are chosen for each sample, denoted as CIGS TF 1, CIGS TF 2, CIGS NTRs 1, and CIGS NTRs 2.

and Se are shown in Figure 4(a) to (d), respectively. Two locations on each sample are randomly chosen in the compositional distributions investigation for statistical information, by which 13 points distributed over 200 nm in depth were analyzed. The findings indicated that the atomic concentration of Cu for CIGS NTRs (below 20%) is lower than that of CIGS TF (20–30%) within a depth of  $\sim 100$  nm. For a region deeper than 50 nm, the atomic concentration of Cu in CIGS NTRs recovers to be the same as that of CIGS TF. In addition, In-rich and Ga-poor compositions were also measured within a depth of  $\sim 25$  nm for CIGS NTRs. This could be due to the low sputtering yield of In and the high sputtering yield of Ga.<sup>18</sup> The drop in atomic concentration of Cu observed in CIGS NTRs can be understood by a region with a lower Cu atomic concentration, namely, a Cu-depletion region, formed after the ion-milling process. The copper-rich secondary phases can be shovelled out by KCN washing, resulting in copper-depleted CIGS NTRs, in which an abundant copper vacancy ( $V_{Cu}$ ) at the surface is expected.

The photocurrent in a CIGS solar cell is drained from abundant point defects in CIGS; therefore defect analysis is crucial for a high-efficiency CIGS absorber layer, for which photoluminescence is the best choice for defect examination.<sup>26,27</sup> Figure 5(a) shows the PL spectra of CIGS TF under excitation powers of 0.01 and

20 mW at 10 K. Five well-resolved PL peaks at 0.84, 0.93, 1.03, 1.11, and 1.14 eV, named p1, p2, p3, p4, and p5, were observed under 0.01 mW at 10 K, while only three PL peaks, namely, p1, p2, and p3, are resolvable under an excitation power of 20 mW at the same excited temperature. Temperature-dependent PL (TD-PL) was also conducted in order to shed light on the activation energies of p1, p2, and p3 *via* Arrhenius plots (see Figure S1). As a result, both p1 and p2 were assigned to donor–acceptor pair (DAP) recombination. The sum of energy levels of donors ( $E_D$ ) and acceptors ( $E_A$ ) related to band edge determines the activation energy at high temperatures ( $E_{a1}$ ), while the shallower energy level related to band edge determines the activation energy at low temperatures ( $E_{a2}$ ).<sup>28</sup> The two DAP recombinations of p1 and p2 share the same shallow donor with  $E_D$  around 10 meV and are distinguished by different acceptors, among which one acceptor has a deeper energy level with  $E_{A1}$  of  $\sim 140$  meV, corresponding to p1, while p2, which is the dominant recombination, has an acceptor with an  $E_{A2}$  of  $\sim 60$  meV. The dominant shallow donor is most likely to be a selenium vacancy ( $V_{Se}$ ) since the existence of  $V_{Se}$  reflects the fact that a slight selenium insufficiency was detected in our samples. Among the two observed acceptors, the one related to p1 is an indium vacancy ( $V_{In}$ ),<sup>29,30</sup> while the other one related to the dominant PL emission, p2, is a

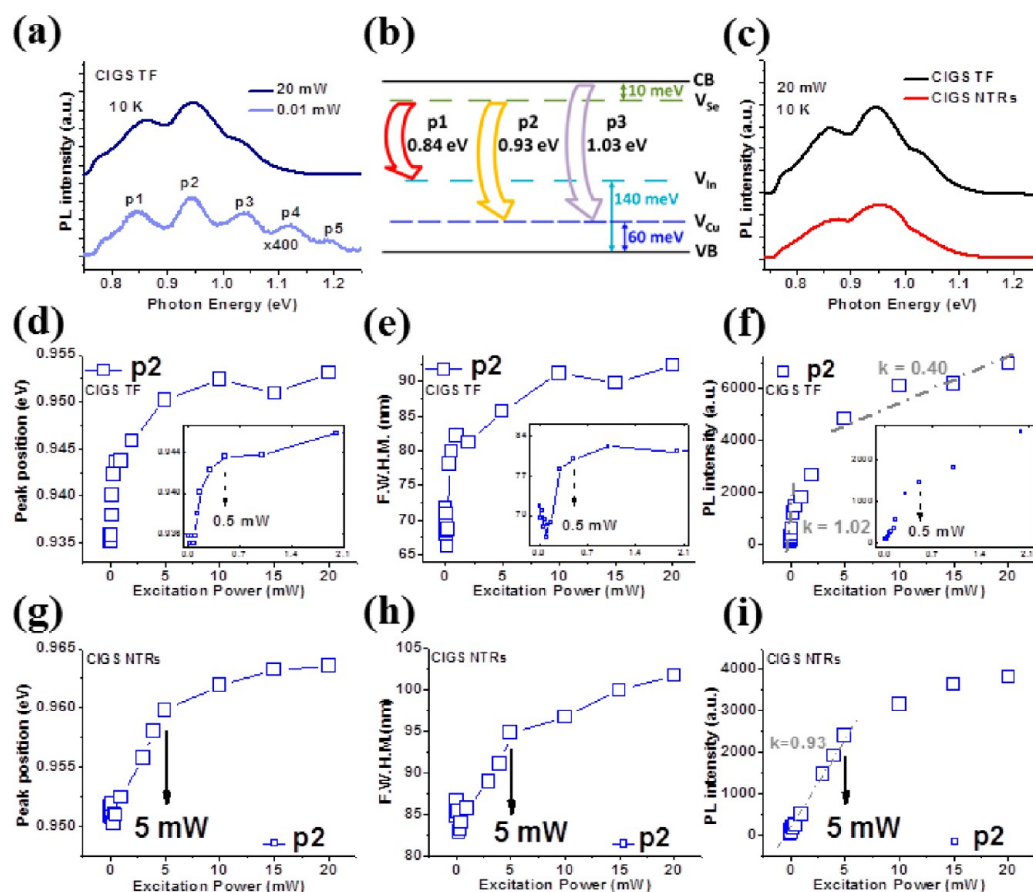


Figure 5. (a) PL spectra of CIGS TF obtained under a low excitation power of 0.01 mW and a high excitation power of 20 mW at 10 K. (b) Energy level diagram of CIGS TF. (c) PL spectra of CIGS TF and CIGS NTRs under 20 mW at 10 K. Change in (d) peak position, (e) fwhm, and (f) PL intensity of p2 depending upon excitation intensity obtained by PL spectral deconvolution of the CIGS TF. Insets show magnifications around 0.5 mW. The same analysis showing (g) peak position, (h) fwhm, and (i) PL intensity of p2 obtained from the CIGS NTRs. (f and i) Results of curve fitting based on  $I \propto L^k$ , in which  $I$  is PL intensity,  $L$  is power of exciting laser radiation, and  $k$  is a constant determined by the recombination mechanism.

copper vacancy ( $V_{Cu}$ ), which possesses the lowest formation energy among all defects in CIGS.<sup>31,32</sup> The emission peak, p3, was related to free-to-acceptor recombination, which has an activation energy  $E_A$  of 60 meV related to a transition from conduction band to acceptor level of  $V_{Cu}$ . Figure 5(b) schematically shows the band diagram constructed according to experimental results. The emission peaks at p4 and p5 under high excitation powers are unresolvable and speculated to be related to a splitting of valence band induced by the tetragonal distortion of the chalcopyrite lattice.<sup>33</sup> PL spectra of CIGS TF and CIGS NTRs obtained under an illumination of 20 mW at 10 K are shown in Figure 5(c). It is evident that the PL emission peaks are broadened after CIGS NTRs were produced through ion-milling. Full width at half-maximum (fwhm) of p1 has been increased from 153.36 nm to 188.96 nm, and that of p2 has been increased from 92.34 nm to 101.63 nm. The photon energy of DAP recombination emission can be expressed as eq 1,<sup>34</sup>

$$E(r) = E_G - (E_A + E_D) + \frac{e^2}{4\pi\epsilon r} \quad (1)$$

where  $E_G$  is the band gap energy,  $e$  is the electronic charge, and  $\epsilon$  is the dielectric constant. In particular, the last term represents Coulomb interaction between DAP and can contribute much as well. For impurity atoms (in our case, point defects in CIGS) occupying normal lattice sites, sharp emission peaks can be observed in the PL spectrum due to the most probable distance between DAP that concentrates the emission energy of each DAP or due to DAP recombination emission irrelevant of DAP separation distance. When the concentration of DAP increases, more distant/closer DAPs or more donors/acceptors that deviate from their original sites can participate in PL emission; therefore the PL emission peak becomes broader due to deviation of their emission energy from the center energy of the PL emission peak. A fwhm expansion of 35.6 nm for p1 and that of 9.29 nm for p2 revealing a higher concentration of DAP have been induced by the ion-milling process, revealing compositional change at the CIGS NTR surface.

DAP concentration can be quantified by power-dependent PL to confirm the increase in DAP concentration. A saturation effect of DAP under low temperature

has been observed *via* PD-PL<sup>35,36</sup> and can be a method for estimation of DAP concentration (see Supporting Information, Figure 2Sa and b). Excitation power dependence of PL emission obeys  $I \propto L^k$ , where  $I$  is PL intensity,  $L$  is the power of exciting laser radiation, and  $k$  is a constant determined by the recombination mechanism.<sup>37</sup> CIGS TF and CIGS NTRs were examined by PD-PL with excitation power varied from 0.01 to 20 mW for estimation of DAP concentration. Among four peaks, p2 shows a distinct saturation effect at both samples. Peak position, fwhm, and PL intensity of p2 for CIGS TF and CIGS NTR samples are accordingly shown in Figure 5(d)–(i). A saturation point has been found to be 0.5 mW, at which the peak position (Figure 5d) undergoes a blue shift and then maintains a constant saturation level after the excitation power reaches 0.5 mW. Also, the fwhm of p2 (Figure 5f) keeps expanding until the excitation power reaches 0.5 mW and then remains constant. The PL intensity (Figure 5i) of p2 exhibits a linear dependence on the excitation power of 0.5 mW with  $k = 1.02$  and eventually shows a sublinear dependence after the excitation power exceeds 0.5 mW with  $k = 0.40$ . In particular, under low excitation powers varied around 0.01 mW, p2 maintains a constant value in peak position (inset in Figure 5d), fwhm (inset in Figure 5e), and PL intensity (inset in Figure 5f) before both the blue shift and the fwhm expansion occur, indicating that PL emission is independent of distance of DAP separation under an excitation power of around 0.01 mW. These observations are in complete accord with the interpretation of DAP saturation under high excitation laser illumination. The PD-PL results of the CIGS NTRs are shown in Figure 5(g), (h), and (i), respectively. Clearly, the DAP saturation level of p2 was found at  $\sim 5$  mW. The peak position shown in Figure 5(g) indicates that blue shift does not stop until reaching a point at  $\sim 5$  mW followed by maintenance at the maximum level. fwhm of p2 as well eventually reaches a constant value until the expansion of the fwhm is stopped at 5 mW as shown in Figure 5(h). The PL emission dependence of p2 stays linear before an excitation power of 5 mW, while a sublinear PL emission dependence was observed under excitation powers beyond 5 mW (Figure 5i).

The transition related to the emission peak at p2, according to the activation energy, is that of  $V_{Se}$  to  $V_{Cu}$ . An increase in concentration of DAP related to p2 infers a higher concentration of  $V_{Se}$  or  $V_{Cu}$  obtained after the ion-milling process. Since p1 emission, which is also related to  $V_{Se}$ , shows no DAP saturation effect,  $V_{Cu}$  is the defect whose concentration is raised after the ion-milling process. In effect, p3, which is related to transition of the conduction band to  $V_{Cu}$ , also shows the DAP saturation effect in PL intensity dependence upon the excitation power. A breakpoint from linear dependence to sublinear dependence has been raised from 0.4 mW to 4 mW (Figure S3). Although the fwhm

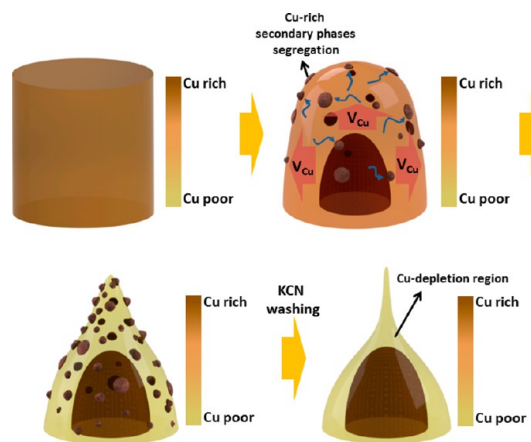


**Figure 6.** Schematic illustration of the formation mechanism of the Cu-depletion region in CIGS NTRs.

and peak position of p3 cannot be extracted due to poor deconvolution of p3 caused by its relatively weak intensity and partial overlapping with p2, the evident change in PL intensity dependence on the excitation power, however, noticeably points out the saturation effect of p3. With the presence of saturation effect revealed from the two  $V_{Cu}$ -related members, p2 and p3, a raise in  $V_{Cu}$  concentration is very likely, which is consistent with the Cu-depletion region proposed according to the EDS results (Figure 4). Additionally, the Cu-depletion region should be formed *via* the Mullins–Sekerka type of instability while ion-milling driven by the diffusion of vacancies out of the bulk alloy,<sup>38,39</sup> thereby raising the concentration of  $V_{Cu}$  at the surface region. The scenario of the formation mechanism of the Cu-depletion region is schematically illustrated in Figure 6. During ion-milling, the surface energy drives the phase segregation in the surface diffusion region, in which  $V_{Cu}$  is aggressively formed due to segregation of copper-rich secondary phases and then is driven to the surface (see the second graph of the sequence in Figure 6). The resultant copper-rich secondary phases at the surface had left a Cu-depletion region behind after CIGS NTRs were formed. The following KCN washing finishes the last step for fabrication of the desired CIGS NTRs for CIGS NTR solar cells (see the last two graphs of the sequence in Figure 6).

The existence of  $V_{Cu}$  allows occupation of Cd atoms on  $V_{Cu}$  sites ( $Cd_{Cu}$ ) as Cd atoms diffuse into the CIGS layer after capping of a CdS layer by chemical bath deposition (CBD).<sup>40–42</sup> Although a detailed mechanism of CIGS/CdS junction remains controversial, CdS diffusion has been widely encouraged for enhancing the device performance by a type-inversed  $Cd_{Cu}$  layer and adjusting the electric field in the space charge region.<sup>43–45</sup> Since a CBD-CdS had been found to be highly resistive so that no heavily doped n-type characteristic has been observed, a buried homojunction due to Cd diffusion at the CIGS/CdS interface that had been reported was believed to be the very location of



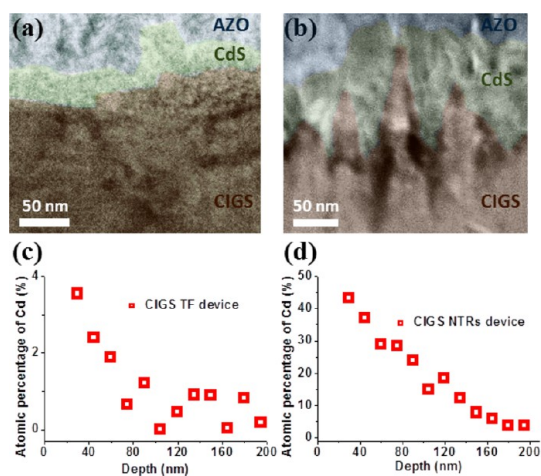


**Figure 7.** TEM images of (a) CIGS TF and (b) CIGS NTR devices. Brown, green, and blue shadows indicate CIGS, CdS, and AZO, respectively. Depth-resolved elementary distribution of Cd in a region extending  $\sim 200$  nm from (c) the CIGS TF surface and (d) the top of a tip of CIGS NTRs in their devices.

the p–n junction in a CIGS solar cell, by which recombination of photogenerated carriers at the CdS/CIGS interface can be avoided by the buried homojunction in bulk.<sup>46,47</sup> Due to an intrinsic property of Cu-poor CIGS, an ordered-vacancy compound (OVC), which is related to a defect complex of  $2V_{Cu} + In_{Cu}$  such as  $Cu_2In_4Se_7$ ,  $CuIn_3Se_5$ , and  $CuIn_5Se_8$ , can be formed with a  $\sim 10$  nm thickness at the surface of CIGS. It behaves as a buffer layer and a type-inversion layer so that a better device performance could be achieved.<sup>48–52</sup> The  $Cd_{Cu}$  layer is capable of playing the same necessary role of type-inversion buffer layer as OVC does.<sup>53,54</sup> Unlike the shallow distribution of OVC at the surface of a CIGS thin film, the  $Cd_{Cu}$  buffer layer can be thicker due to the deeper penetration of Cd diffusion.<sup>55</sup> Cd diffusion also allows passivation at the CdS/CIGS interface. Therefore, Cd diffusion is able to effectively reduce recombination centers by a buried p–n junction in CIGS bulk. The buried p–n junction can also avoid factors affecting the CdS/CIGS interface that weaken built-in potential in the depletion region, such as impurities or weak adhesion of CdS to CIGS. Such benefits can result in enhanced  $V_{OC}$  and FF of the CIGS NTR solar cell, as shown in Figure 3(a). In CIGS NTRs shown here, the increase in  $V_{Cu}$  concentration encouraged Cd diffusion and consequently enhanced the device efficiency.

To verify the difference in Cd diffusion, EDS was performed on CIGS TF and CIGS NTR devices to check the quantitatively depth-resolved compositional distributions of Cd. Figure 7(a) and (b) show TEM images of CIGS TF and CIGS NTR devices at the CIGS/CdS interface, in which brown, green, and blue shadows indicate CIGS, CdS, and AZO, respectively. Figure 7(c) and (d) show results of depth-resolved Cd distribution. A depth around 200 nm in CIGS was investigated for the two devices. For the CIGS TF device, only 4% at maximum atomic concentration of Cd concentration

was detected in the CIGS TF and vanished at a depth of  $\sim 80$ – $100$  nm. On the contrary, a maximum atomic concentration of Cd up to  $\sim 45\%$  was detected in CIGS NTRs, and Cd diffusion has been found to extend by a depth of  $\sim 180$  nm into the bulk. The resultant Cd diffusion length of  $\sim 180$  nm is contributed from both the ion-milling-generated Cu-depletion region of  $\sim 100$  nm in depth and additional Cd diffusion extending  $\sim 100$  nm further due to the intrinsic characteristic of CIGS TF.

By taking advantage of an enhanced Cd diffusion, the p–n junction with CIGS NTRs has better electrical properties compared to that of CIGS TF. This can be examined by time-resolved photoluminescence (TRPL). TRPL measurements at 10 K were conducted at the CIGS/CdS p–n junctions of CIGS TF and CIGS NTRs. Both samples showed biexponential decay in PL intensity, in which the values of lifetime for fast and slow components,  $\tau_1$  and  $\tau_2$ , were 25.93 and 202.49 ns for the CIGS TF, respectively, while those of the CIGS NTRs were found to be 25.93 and 232.15 ns, respectively (see Figure S4). This is a proof of a better built-in electrical field profile due to a space charge region shifted into the CIGS bulk. Through these improvements, less current loss is expected in a direct-sputtered CIGS solar cell with CIGS NTRs due to less recombination in the depletion region compared to the one made of CIGS TF.

In order to confirm that the better performance of the CIGS NTR device is due to non-illumination-related benefits, the electrical properties of the CIGS TF device and CIGS NTRs device are investigated by dark current  $J$ – $V$  measurements. Figure 8(a) and (b) show the dark current  $J$ – $V$  curves of the CIGS TF and NTRs at 25 and 120  $^{\circ}C$ , respectively. When under a lower forward bias voltage (from 0 to 0.4–0.5 V) at both 25 and 120  $^{\circ}C$ , the forward current of the CIGS NTRs is evidently lower, indicating less shunt leakage for the CIGS NTR device compared to that of the CIGS TF device.<sup>56,57</sup> It is due to less recombination of photogenerated carriers in the p–n junction. One common side effect of solar cells with the nanopatterned p–n junction is deterioration in electrical performance due to bad coverage and adhesion of the capping layer onto the patterned substrate. Yet, chemical bath deposition, the conventional method for CdS deposition, possesses a good adaptability to a rough surface. The advantage allows the benefits of CIGS NTRs not to be overwhelmed by deterioration in electrical performance but lead to the further suppression of shunt leakage. In addition, the forward current of the CIGS NTRs at both 25 and 120  $^{\circ}C$  under a large forward bias (larger than 0.4–0.5 V) has been found to surpass that of the CIGS TF (Figure 8(a) and (b)). This reflects that a greater contribution of diode current is dominant in the CIGS NTRs compared to that of the CIGS TF and suggests a lower series resistance.<sup>56–58</sup> It could be the enlarged area of the p–n junction on the CIGS NTRs that boosts the

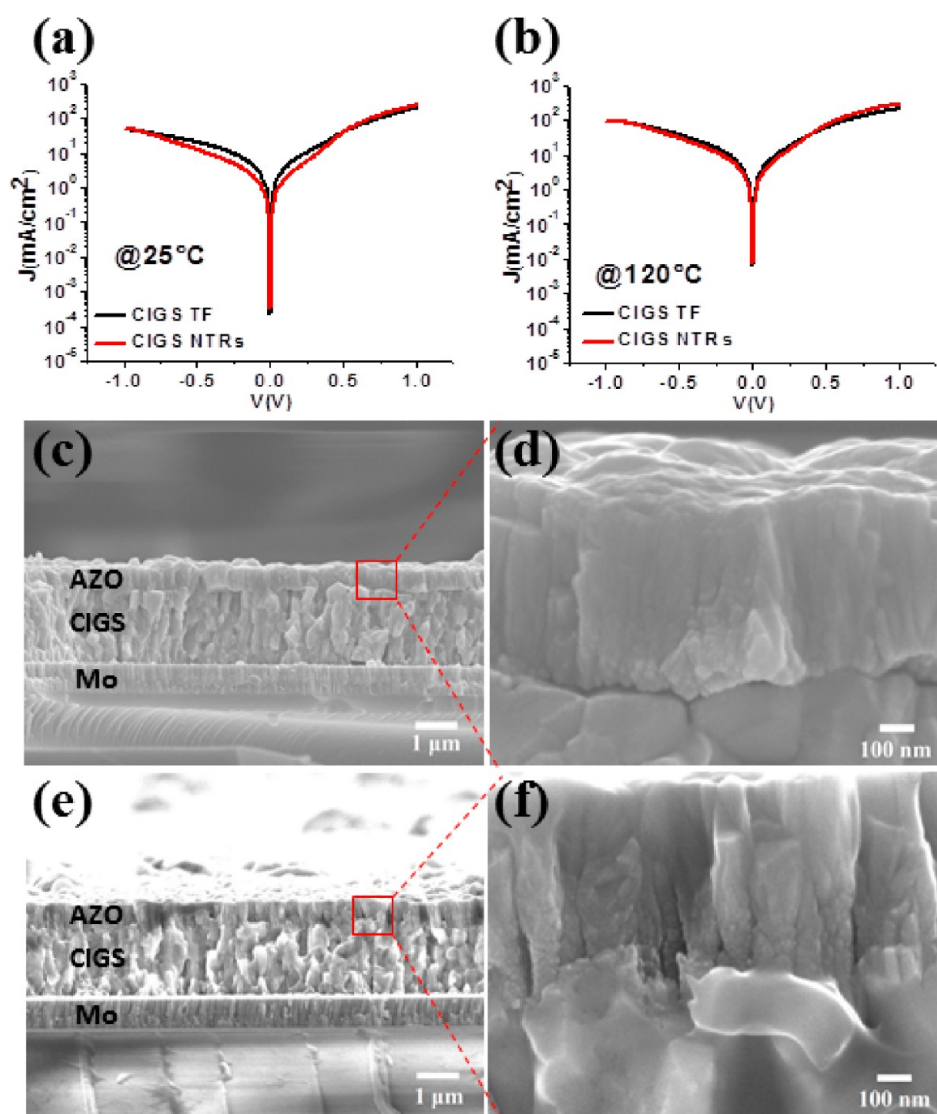


**Figure 8.**  $J$ – $V$  curves of dark current obtained from the CIGS TF device, which is shown as a black line, and that of the CIGS NTRs device, which is shown as a red line, measured at (a) 25 °C and (b) 120 °C, respectively. (c) Cross-section SEM image of CIGS TF solar cell and (d) its magnification images at the CIGS/CdS interface. (e) Cross-section SEM image of an NTR solar cell and (f) its magnification images at the CIGS/CdS interface.

generation of diode current. In addition, the AZO thin film shows better adhesion on the nanotextured CIGS surface rather than on the nontextured CIGS surface. Figure 8(c) and (e) show the cross section SEM images of the CIGS TF and NTRs, while Figure 8(d) and (f) show their magnified images of the interface between AZO and CIGS, respectively. Obviously, a gap between AZO and CIGS TF can be observed throughout the junction. On the contrary, due to better adhesion of AZO on the CIGS NTRs, no sign of such a gap can be found (Figure 8(e) and (f)). The better adhesion of AZO in the CIGS NTRs can be due to the conical-shaped textured surface of the CIGS NTRs, which had tightly bonded with the AZO thin film, resulting in the reduction of the lower series resistance. The decrease in shunt leakage and series resistance due to enhanced Cd diffusion explained why  $V_{OC}$  and FF of the CIGS NTRs device have been enhanced,<sup>59</sup> as shown in Figure 3. It has revealed

the main contribution of efficiency boost by the CIGS NTRs scheme.

Usually, significant resultant surface defects behaving as nonradiative recombination centers need to be taken into account in micro/nanostructured device fabrication. Luckily, point defects in CIGS exhibit as donors and acceptors, which are crucial to provide carriers; therefore the existence of point defects is allowed. For the CIGS, most etching processes provide different elementary etching yields; as a result, elementary concentrations in the CIGS, hence point defect concentrations, can be changed and lead to modification in surface carrier concentration of CIGS and its device performance. Such factors need to be considered and properly utilized. By the perspective given in this work, a new approach to efficiency enhancement in a nanopatterned CIGS solar cell has been proposed.

## CONCLUSION

We have presented a systematic work that examines the effects of CIGS NTRs obtained *via* ion-milling on direct-sputtered CIGS solar cells. Large-area CIGS NTRs has been successfully fabricated, and characteristics differing from CIGS TF have been investigated. After KCN washing, a shallow region at the surface with a lower copper concentration has been discovered in CIGS NTRs *via* EDS results. This is a consequence of surface diffusion ignited by ion-bombardment, which causes copper-rich secondary phase segregation at the surface. After KCN washing, removal of secondary phases can be achieved, and a layer with abundant  $V_{Cu}$  was left behind. Examinations by PD-PL support such an inference by exhibition of an increase in the concentration of  $V_{Cu}$ . Such a compositional change can be a benefit for a CIGS solar cell by promoting formation of  $Cd_{Cu}$  at a CdS/CIGS interface to enhance

interface passivation as well as carrier extraction.  $Cd_{Cu}$  has also been verified by EDS. By TRPL at 10 K, a longer lifetime has been observed in the CdS/CIGS junction with CIGS NTRs, indicating a better carrier extraction. According to the dark current of direct-sputtered CIGS solar cells with and without CIGS NTRs, it has been found that the shunt leakage of the device with CIGS NTRs has been effectively suppressed by CIGS NTRs. The decrease in shunt leakage due to CIGS NTRs accords well with the inference established on the results of EDS and PD-PL. Series resistance has also been found to be decreased in the presence of CIGS NTRs. This could be due to the better adhesion of the AZO layer on the surface textured by CIGS NTRs, which is confirmed by cross-section SEM images. These systematic analyses have shown the the main sources providing enhancement in efficiency *via* CIGS NTRs and have excluded antireflection from the major factors.

## EXPERIMENTAL METHODS

**Device Fabrications.** CIGS thin films were directly deposited from a single quaternary CIGS target synthesized by sintering a uniform mixture of  $Cu_2Se$ ,  $In_2Se_3$ , and  $Ga_2Se_3$  powders with particle size less than  $50\ \mu m$  at  $600\text{--}800\ ^\circ C$  and  $300\text{--}400$  bar for 3 h. The CIGS thin films were deposited on a Soda Lime Glass (SLG) coated with an 800 nm thick Mo layer at  $500\ ^\circ C$ . The quaternary CIGS target is a chalcopyrite phase and contains 24.3% Cu, 18.7% In, 7.8% Ga, and 49.2% Se, respectively. To form large-area NTRs, the CIGS TF were sent into a vacuum ion-milling chamber with a 4 in. working area and were bombarded for one hour at normal incidence with  $Ar^+$  ions under an accelerated voltage of 0.3 kV at a vacuum pressure of  $1.2 \times 10^{-4}$  Torr. Consequently, large-area and normally oriented CIGS NTRs were produced. An immersion in 10% KCN solution for 10 minutes was applied to all samples. For examinations of electrical properties, two samples with NTRs and without NTRs were fabricated into devices. Device structures are Al:ZnO (AZO, 250 nm)/ZnO (80 nm)/CdS (50 nm for CIGS TF device, 100 nm for CIGS NTRs device)/CIGS (2000 nm)/Mo (800 nm)/SLG.

**Characterization.** For PL and TRPL measurements, a 635 nm diode laser was used. During temperature-dependent PL, the temperature was varied from 10 to 300 K under an excitation power of 20 mW. On the other hand, power-dependent PL was carried out at 10 K with excitation powers ranging from 0.01 to 20 mW. The PL signal emitted from the CIGS sample was transferred to a monochromator with 600 groove/mm grating and detected by an infrared photomultiplier tube. TRPL was conducted by a pulsed semiconductor laser with a center wavelength of 635 nm, fwhm of 76 ps, and frequency of 80 MHz.

For characterization measurements of the devices and thin films, the following instruments were utilized. A UV–vis–NIR spectrophotometer (Hitachi U4100) with standard mirror optics and an integrating sphere was used to measure the specular reflectance of CIGS solar cells in the 400–1200 nm range at normal incidence.  $J$ – $V$  measurements were performed, closely following the procedure described in international standard CEI IEC 60904-1. Both the solar cells and the reference cell were characterized under a simulated Air Mass 1.5, Global (AM1.5G) illumination with a power of  $1000\ W/m^2$ . The temperature was actively controlled during the measurements and was  $25 \pm 1\ ^\circ C$ . The power conversion efficiency (PCE) measurement system consisted of a power supply (Newport 69920), a 1000 W Class A solar simulator (Newport 91192A) with a xenon lamp (Newport 6271A), an AM1.5G filter (Newport 81088A), a probe stage, and a source-meter with a four-wire mode (Keithley 2400). In the

calibration report by Newport Corporation, the temporal instability was 0.88% and the nonuniformity was 0.79%. The spectrum of the solar simulator was measured by a calibrated spectroradiometer (Soma S-2440) in the wavelength range of 300 to 1100 nm. The external quantum efficiency system employed a 300 W xenon lamp (Newport 66984) light source and a monochromator (Newport 74112). A calibration was performed using a calibrated silicon photodetector with a reported spectral response (Newport 818-UV). The EQE measurement was carried out using a lock-in amplifier (Standard Research System, SR830), an optical chopper unit (SR540) operated at 260 Hz chopping frequency, and a  $1\ \Omega$  resistor in shunt connection to convert the photocurrent into voltage.

**Conflict of Interest:** The authors declare no competing financial interest.

**Acknowledgment.** This research was supported by the National Science Council through Grant Nos. 101-2622-E-007-011-CC2, 101-2622-E-492-001-CC2, and NSC 101-2218-E-007-009-MY3 and the National Tsing Hua University through Grant No. 102N2022E1. Y.L.C. greatly appreciates the use of the facility at CNMM, National Tsing Hua University, through Grant No. 102N2744E1.

**Supporting Information Available:** Arrhenius plots of PL spectra of CIGS TF; schematic illustration of donor–acceptor pair saturation effect upon power-dependent PL measurements; PL intensity dependence upon excitation power of p3 in PL spectra obtained from CIGS TF and CIGS NTRs; PL intensity decays of p2 obtained from CIGS TF and CIGS NTRs with CdS capping the top of both samples. These materials are available free of charge *via* the Internet at <http://pubs.acs.org>.

## REFERENCES AND NOTES

- Dimmler, B. CIGS and CdTe Based Thin Film PV Modules, an Industrial Revolution. *Proc. 37th IEEE Photovoltaic Spec. Conf.* **2011**, 2011, 002494–002495.
- EMPA. Rekordwirkungsgrad von 20.4% für Flexible Solarzellen. *Vak. Forsch. Prax.* **2013**, 25, 26.
- Jackson, P.; Hariskos, D.; Lotter, E.; Paetel, S.; Wuerz, R.; Menner, R.; Wischmann, W.; Powalla, M. New World Record Efficiency for  $Cu(In,Ga)Se_2$  Thin-Film Solar Cells Beyond 20%. *Prog. Photovoltaics: Res. Appl.* **2011**, 19, 894–897.
- Chang, J. C.; Chuang, C. C.; Guo, J. W.; Hsu, S. C.; Hsu, H. R.; Wu, C. S.; Hsieh, T. P. An Investigation of  $CuInGaSe_2$  Thin Film Solar Cells by Using  $CuInGa$  Precursor. *Nanosci. Nanotechnol. Lett.* **2011**, 3, 200–203.



5. Kapur, V. K.; Bansal, A.; Le, P.; Asensio, O. I. Non-Vacuum Processing of  $\text{CuIn}_{1-x}\text{Ga}_x\text{Se}_2$  Solar Cells on Rigid and Flexible Substrates Using Nanoparticle Precursor Inks. *Thin Solid Films* **2003**, 431–432, 53–57.
6. Calixto, M. E.; Dobson, K. D.; McCandless, B. E.; Birkmire, R. W. Controlling Growth Chemistry and Morphology of Single-Bath Electrodeposited  $\text{Cu}(\text{In,Ga})\text{Se}_2$  Thin Films for Photovoltaic Application. *J. Electrochem. Soc.* **2006**, 153, G521–G528.
7. Chen, C. H.; Hsu, C. H.; Chien, C. Y.; Wu, Y. H.; Lai, C. H. A Straightforward Method to Prepare Chalcopyrite CIGS Films by One-Step Sputtering Process without Extra Se Supply. *Proc. 37th IEEE Photovoltaic Spec. Conf.* **2011**, 2011, 002687–002690.
8. Chang, Y. J.; Chen, Y. T. Broadband Omnidirectional Antireflection Coatings for Metal-Backed Solar Cells Optimized Using Simulated Annealing Algorithm Incorporated with Solar Spectrum. *Opt. Express* **2011**, 19, A875–A887.
9. Chi, F. T.; Yan, L. H.; Lu, H. B.; Yan, H. W.; Yuan, X. D.; Jiang, B. Sol-Gel Preparation of Ultralow Refractive Index Magnesium Fluoride Optical Films for Broadband Antireflective Coatings. *Nanosci. Nanotechnol. Lett.* **2012**, 4, 441–444.
10. Yoshida, A. Antireflection of the Butterfly and Moth Wings through Microstructure. *Forma* **2002**, 17, 75–89.
11. Wilson, S. J.; Hutley, M. C. The Optical Properties of 'Moth Eye' Antireflection Surfaces. *Opt. Acta* **1982**, 29, 993–1009.
12. Huang, Y. F.; Chattopadhyay, S.; Jen, Y. J.; Peng, C. Y.; Liu, T. A.; Hsu, Y. K.; Pan, C. L.; Lo, H. C.; Hsu, C. H.; Chang, Y. H.; *et al.* Improved Broadband and Quasi-Omnidirectional Anti-Reflection Properties with Biomimetic Silicon Nanostructures. *Nat. Nanotechnol.* **2007**, 2, 770–774.
13. Tseng, P. C.; Tsai, M. A.; Yu, P.; Kuo, H. C. Antireflection and Light Trapping of Subwavelength Surface Structures Formed by Colloidal Lithography on Thin Film Solar Cells. *Prog. Photovoltaics: Res. Appl.* **2012**, 20, 135–142.
14. Tsai, M. A.; Tseng, P. C.; Chen, H. C.; Kuo, H. C.; Yu, P. Enhanced Conversion Efficiency of a Crystalline Silicon Solar Cell with Frustum Nanorod Arrays. *Opt. Express* **2011**, 19, A28–A34.
15. Tseng, P. C.; Yu, P.; Chen, H. C.; Tsai, Y. L.; Han, H. W.; Tsai, M. A.; Chang, C. H.; Kuo, H. C. Angle-Resolved Characteristics of Silicon Photovoltaics with Passivated Conical-Frustum Nanostructures. *Sol. Energy Mater. Sol. Cells* **2011**, 95, 2610–2615.
16. Chen, T. G.; Yu, P.; Tsai, Y. L.; Shen, C. H.; Hsieh, C. M.; Tsai, M. A.; Kuo, H. C. Nano-Patterned Glass Superstrates with Different Aspect Ratios for Enhanced Light Harvesting in a-Si:H Thin Film Solar Cells. *Opt. Express* **2012**, 20, A412–A417.
17. Ni, J.; Li, Z. C.; Zhou, Q.; Zhang, Z. J.; Wei, B. Q. Thermal Stability of  $\text{HfO}_2$  Nanostructures as Antireflection Coatings. *Nanosci. Nanotechnol. Lett.* **2011**, 3, 731–734.
18. Liu, C. H.; Chen, C. H.; Chen, S. Y.; Yen, Y. T.; Kuo, W. C.; Liao, Y. K.; Juang, J. Y.; Kuo, H. C.; Lai, C. H.; Chen, L. J.; *et al.* Large Scale Single-Crystal  $\text{Cu}(\text{In,Ga})\text{Se}_2$  Nanotip Arrays For High Efficiency Solar Cell. *Nano Lett.* **2011**, 11, 4443–4448.
19. Hsieh, M. Y.; Kuo, S. Y.; Han, H. V.; Yang, J. F.; Liao, Y. K.; Lai, F. I.; Kuo, H. C. Enhanced Broadband and Omnidirectional Performance of  $\text{Cu}(\text{In,Ga})\text{Se}_2$  Solar Cells with ZnO Functional Nanotree Arrays. *Nanoscale* **2013**, 5, 3841–3846.
20. Sigmund, P. Theory of Sputtering. I. Sputtering Yield of Amorphous and Polycrystalline Targets. *Phys. Rev.* **1969**, 184, 383–416.
21. Balefs, G. S.; Bruinsma, R.; Eklund, E. A.; Karunasiri, R. P. U.; Rudnick, J.; Zangwill, A. Growth and Erosion of Thin Solid Films. *Science* **1990**, 249, 264–268.
22. Facsko, S.; Dekorsy, T.; Koerdert, C.; Trappe, C.; Kurz, H.; Vogt, A.; Hartnagel, H. L. Formation of Ordered Nanoscale Semiconductor Dots by Ion Sputtering. *Science* **1999**, 285, 1551–1553.
23. Le Roy, S.; Barthel, E.; Brun, N.; Lelarge, A.; Søndergård, E. Self-Sustained Etch Masking: A General Concept to Initiate the Formation of Nanopatterns During Ion Erosion. *J. Appl. Phys.* **2009**, 106, 094308.
24. Le Roy, S.; Søndergård, E.; Nerbø, I. S.; Kildemo, M.; Plapp, M. Diffuse-Interface Model for Nanopatterning Induced by Self-Sustained Ion-Etch Masking. *Phys. Rev. B* **2010**, 81, 161401.
25. Li, J.; Stein, D.; McMullan, C.; Branton, D.; Aziz, M. J.; Golovchenko, J. A. Ion-Beam Sculpting at Nanometre Length Scales. *Nature* **2001**, 412, 166–169.
26. Rega, N.; Siebentritt, S.; Albert, J.; Nishiwaki, S.; Zajogin, A.; Lux-Steiner, M. Ch.; Kniese, R.; Romero, M. J. Excitonic Luminescence of  $\text{Cu}(\text{In,Ga})\text{Se}_2$ . *Thin Solid Films* **2005**, 480–481, 286–290.
27. Johnson, P. K.; Heath, J. T.; Cohen, J. D.; Ramanathan, K.; Sites, J. R. A Comparative Study of Defect States in Evaporated and Selenized CIGS(S) Solar Cells. *Prog. Photovoltaics: Res. Appl.* **2005**, 13, 579–586.
28. Töpfer, K.; Bruns, J.; Scheer, R.; Weber, M.; Weidinger, A.; Bräunig, D. Photoluminescence of  $\text{CuInS}_2$  Thin Films and Solar Cells Modified by Postdeposition Treatments. *Appl. Phys. Lett.* **1997**, 71, 482–484.
29. Dirnsdorfer, I.; Hofmann, D. M.; Meister, D.; Meyer, B. K.; Riedl, W.; Karg, F. Postgrowth Thermal Treatment of  $\text{CuIn}(\text{Ga})\text{Se}_2$ : Characterization of Doping Levels in In-Rich Thin Films. *J. Appl. Phys.* **1999**, 85, 1423–1428.
30. Wagner, M.; Dirnsdorfer, I.; Hofmann, D. M.; Lampert, M. D.; Karg, F.; Meyer, B. K. Characterization of  $\text{CuIn}(\text{Ga})\text{Se}_2$  Thin Films. *Phys. Status Solidi A* **1998**, 167, 131–142.
31. Bauknecht, A.; Siebentritt, S.; Albert, J.; Lux-Steiner, M. Ch. Radiative Recombination via Intrinsic Defects in  $\text{Cu}_x\text{Ga}_{1-x}\text{Se}_2$ . *J. Appl. Phys.* **2011**, 89, 4391–4400.
32. Zhang, S. B.; Wei, S. H.; Zunger, A.; Katayama-Yoshida, H. Defect Physics of the  $\text{CuInSe}_2$  Chalcopyrite Semiconductor. *Phys. Rev. B* **1998**, 57, 9642–9656.
33. Mudryi, A. V.; Victorov, I. A.; Gremenok, V. F.; Patuk, A. I.; Shakin, I. A.; Yakushev, M. V. Optical Spectroscopy of Chalcopyrite Compounds  $\text{CuInS}_2$ ,  $\text{CuInSe}_2$  and Their Solid Solutions. *Thin Solid Film* **2003**, 431–432, 197–199.
34. Varshni, Y. P. Temperature Dependence of the Energy Gap in Semiconductors. *Physica* **1967**, 34, 149–154.
35. Thomas, D. G.; Gershenson, M.; Trumbore, F. A. Pair Spectra and "Edge" Emission in Gallium Phosphide. *Phys. Rev.* **1964**, 133, A269–A279.
36. Maeda, K. Temperature Dependence of Pair Band Luminescence in GaP. *J. Phys. Chem. Solids* **1965**, 26, 595–605.
37. Schmidt, T.; Lischka, K.; Zulehner, W. Excitation-Power Dependence of the Near-Band-Edge Photoluminescence of Semiconductors. *Phys. Rev. B* **1992**, 45, 8989–8994.
38. Plapp, M.; Gouyet, J. F. Surface Modes and Ordered Patterns during Spinodal Decomposition of an ABv Model Alloy. *Phys. Rev. Lett.* **1997**, 78, 4970–4973.
39. Mullins, W. W.; Sekerka, R. F. Stability of a Planar Interface during Solidification of a Dilute Binary Alloy. *Phys. Rev. Lett.* **1964**, 35, 444–451.
40. Heske, C.; Eich, D.; Fink, R.; Umbach, E.; Buuren, T. V.; Bostedt, C.; Terminello, L. J.; Kakar, S.; Grush, M. M.; Callcott, T. A.; *et al.* Observation of Intermixing at the Buried  $\text{CdS}/\text{Cu}(\text{In,Ga})\text{Se}_2$  Thin Film Solar Cell Heterojunction. *Appl. Phys. Lett.* **1999**, 74, 1451–1453.
41. Shirakata, S.; Nakada, T. Photoluminescence and Time-Resolved Photoluminescence in  $\text{Cu}(\text{In,Ga})\text{Se}_2$  Thin Films and Solar Cells. *Phys. Status Solidi C* **2009**, 6, 1059–1062.
42. Nakada, T.; Kunioka, A. Direct Evidence of Cd Diffusion into  $\text{Cu}(\text{In,Ga})\text{Se}_2$  Thin Films During Chemical-Bath Deposition Process of  $\text{CdS}$  Films. *Appl. Phys. Lett.* **1999**, 74, 2444–2446.
43. Ramanathan, K.; Hasoon, F. S.; Smith, S.; Young, D. L.; Contreras, M. A.; Johnson, P. K.; Pudov, A. O.; Sites, J. R. Surface Treatment of  $\text{CuInGaSe}_2$  Thin Films and Its Effect on the Photovoltaic Properties of Solar Cells. *J. Phys. Chem. Solids* **2003**, 64, 1495–1498.
44. Raw, U.; Schmidt, M. Electronic Properties of  $\text{ZnO}/\text{CdS}/\text{Cu}(\text{In,Ga})\text{Se}_2$  Solar Cells—Aspects of Heterojunction Formation. *Thin Solid Films* **2001**, 387, 141–146.
45. Contreras, M. A.; Romero, M. J.; To, B.; Hasoon, F.; Noufi, R.; Ward, S.; Ramanathan, K. Optimization of CBD  $\text{CdS}$  Process in High-Efficiency  $\text{Cu}(\text{In,Ga})\text{Se}_2$ -Based Solar Cells. *Thin Solid Films* **2002**, 403–404, 204–211.



46. Yu, P. H.; Faile, S. P.; Park, Y. S. Cadmium-Diffused  $\text{CuInSe}_2$  Junction Diode and Photovoltaic Detection. *Appl. Phys. Lett.* **1975**, *26*, 384–385.
47. Jiang, C. S.; Hasoon, F. S.; Moutinho, H. R.; Al-Thani, H. A.; Romero, M. J.; Al-Jassim, M. M. Direct Evidence of a Buried Homojunction in  $\text{Cu(In,Ga)Se}_2$  Solar Cells. *Appl. Phys. Lett.* **2003**, *82*, 127–129.
48. Zhang, S. B.; Wei, S. H.; Zunger, A. Stabilization of Ternary Compounds via Ordered Arrays of Defect Pairs. *Phys. Rev. Lett.* **1997**, *78*, 4059–4062.
49. Schmid, D.; Ruckh, M.; Schok, H. W. A Comprehensive Characterization of the Interfaces in  $\text{Mo/CIS/CdS/ZnO}$  Solar Cell Structures. *Sol. Energy Mater. Sol. Cells* **1996**, *41/42*, 281–294.
50. Dharmadasa, I. M. Fermi Level Pinning and Effects on  $\text{CuInGaSe}_2$ -Based Thin-Film Solar Cells. *Semicond. Sci. Technol.* **2009**, *24*, 055016.
51. Minemoto, T.; Matsui, T.; Takakura, H.; Hamakawa, Y.; Negami, T.; Hashimoto, Y.; Uenoyama, T.; Kitagawa, M. Theoretical Analysis of the Effect of Conduction Band Offset of Window/CIS Layers on Performance of CIS Solar Cells Using Device Simulation. *Sol. Energy Mater. Sol. Cells* **2001**, *67*, 83–88.
52. Schmid, D.; Ruckh, M.; Grunwald, F.; Schock, H. W. Chalcopyrite/Defect Chalcopyrite Heterojunctions on the Basis of  $\text{CuInSe}_2$ . *J. Appl. Phys.* **1993**, *73*, 2902–2909.
53. Liao, D.; Rockett, A. Cu Depletion at the  $\text{CuInSe}_2$  Surface. *Appl. Phys. Lett.* **2003**, *82*, 2829–2831.
54. Park, S. W.; Park, S. Y.; Lee, E. W.; Jung, W. J.; Jeon, C. W.; Chung, Y. D.; Park, N. M.; Kim, J. Dependence of  $\text{Cu(In,Ga)Se}_2$  Solar Cell Performance on Cd Solution Treatment Conditions. *Mol. Cryst. Liq. Cryst.* **2011**, *551*, 221–227.
55. Liao, D.; Rockett, A. Cd Doping at the  $\text{CuInSe}_2/\text{CdS}$  Heterojunction. *J. Appl. Phys.* **2003**, *93*, 9380–9382.
56. Liao, Y. K.; Kuo, S. Y.; Hsieh, M. Y.; Kao, M. H.; Cheng, S. J.; Chiou, D. W.; Hsieh, T. P.; Kuo, H. C. A Look into the Origin of Shunt Leakage Current of  $\text{Cu(In,Ga)Se}_2$  Solar Cells via Experimental and Simulation Methods. *Sol. Energy Mater. Sol. Cells* **2013**, *117*, 145–151.
57. Dongaonkar, S.; Servais, J. D.; Ford, G. M.; Loser, S.; Moore, J.; Gelfand, R. M.; Mohseni, H.; Hillhouse, H. W.; Agrawal, R.; Ratner, M. A.; et al. Universality of Non-Ohmic Shunt Leakage in Thin-Film Solar Cells. *J. Appl. Phys.* **2010**, *108*, 124509.
58. Tan, J. H.; Anderson, W. A. Current Transport in Copper Indium Gallium Diselenide Solar Cells Comparing Mesa Diodes to the Full Cell. *Sol. Energy Mater. Sol. Cells* **2003**, *77*, 283–292.
59. Ramanathan, K.; Noufi, R.; Granata, J.; Webb, J.; Keane, J. Prospects for *in Situ* Junction Formation in  $\text{CuInSe}_2$  Based Solar Cells. *Sol. Energy Mater. Sol. Cells* **1998**, *55*, 15–22.